JMEPEG (2016) 25:3725–3736
DOI: 10.1007/s11665-016-2232-z

1059-9495/$19.00

Flow Stress Analysis and Hot Bending of P11 Alloy Steel

Fu-ye Ma, Kai Jin, Hui Wang, Wen-Jiao Pei, Xiao-Bin Tang, Jie Tao, and Xun-Zhong Guo

(Submitted February 25, 2016; in revised form June 29, 2016; published online July 18, 2016)

Based on the growing application value of the P11 alloy steel in the nuclear power field, its dynamic recrystallization (DRX) behavior was firstly investigated by means of isothermal hot compression experiments, under the conditions of a testing temperature range between 800 and 950 °C, and a strain rate range between 0.01 and 2/s. Furthermore, optical microscopy and transmission electron microscopy were also employed to analyze the effect of the mechanism of the strain rate on DRX. The results indicated that the grain size could be significantly refined with the increase of strain rate. Also, the recrystallized volume fraction was increased and the dislocation density decreased with the decrease of strain rate, for the same strain values. Subsequently, numerical simulations, under the assistance of experimental results on DRX behavior, were successfully used to study the hot push bending process and simultaneously obtain the processing parameters of the actual work-pieces. Finally, some comparative analyses were performed and discussed in parallel with the deformed actual work-pieces. The EBSD results on the deformed P11 alloy steel were emphasized for exploring the forming properties of this alloy steel.

Keywords dynamic recrystallization, hot push bending, ox-horn core bar, P11 alloy steel, strain rate

1. Introduction

In recent years, the newly built nuclear power stations, represented by AP1000, mostly adopt the advanced pressurized water reactor (PWR) technique (Ref 1). The piping material used for heat transfer for the PWR is characterized by higher resistance against pressure and temperature, longer designed life, and superior high-temperature mechanical properties. The piping material for PWR should exhibit high corrosion resistance and excellent mechanical strength. As one of the main piping materials for PWR, P11 alloy steel could be effectively utilized in higher temperature environments and corrosive media, withstanding higher flow rates (as high as 50 m/s), due to the excellent abrasion resistance and corrosion resistance. Furthermore, this alloy steel exhibits interesting performance characteristics and is also extensively used in extraction steam lines and crude distillation units.

During the thermoplastic formation of P11 alloy steel, the parameters involved in the hot working process influence the dynamic recovery and recrystallization (Ref 2, 3). Dynamic recrystallization (DRX), the most important phenomenon in the hot deformation process regarding the microstructural evolution, can improve the mechanical properties of the material through grain refining, eliminating the dislocations and microcracks caused by work hardening of the materials (Ref 4-9).

In this study, hot compression tests were performed to analyze the hot deformation behavior of P11 alloy steel and to obtain the critical conditions for DRX. Furthermore, the effects of the strain rates on the DRX structure during hot deformation were studied to provide a deeper understanding of the hot deformation behavior of P11 alloy steel. Finally, the hot push bending process was also performed on P11 alloy steel tubes and the microstructure and mechanical properties of the tube were studied through EBSD analysis.

2. Flow Stress Analysis of P11 Alloy Steel

The elemental composition of P11 alloy steel is listed in Table 1. Cylindrical specimens with diameter of 10 mm and height of 12 mm were prepared to perform the compression tests, according to the ANSI/ASTM E 209-2000 standard. The hot compression tests were performed on a Gleeble-3500 thermal simulation testing machine, with a maximum load capacity and live load of 100 and 60 KN, respectively. The testing machine specimens before and after compression are presented in Fig. 1.

Based on the actual forming temperature of P11 alloy steel, the temperatures for the compression tests were selected in the range between 800 and 950 °C with an interval of 50 °C and the strain rates were set as 0.01, 0.1, 1, or 2/s. Prior to hot deformation, the specimens were heated to the compression testing temperature at a rate of 10 °C/s and held for 5 min to eliminate any thermal gradients and ensure the uniformity of the temperature. Subsequently, a height reduction of 60% was achieved until the end of the compression tests. In the process

Fu-ye Ma, Jie Tao, and **Xun-Zhong Guo**, Institute of Advanced Materials and Forming Technology, NUAA, Nanjing 211100, People's Republic of China; Jiangsu Key Laboratory of Nuclear Energy Equipment Materials Engineering, Nanjing 211100, People's Republic of China; and College of Material Science and Technology, Nanjing University of Aeronautics and Astronautics, Nanjing 211100, People's Republic of China; **Kai Jin**, Sogang University, Department of Mechanical Engineering, Seoul, 121-742, Korea; **Hui Wang**, Institute of Advanced Materials and Forming Technology, NUAA, Nanjing 211100, People's Republic of China; and Jiangsu Key Laboratory of Nuclear Energy Equipment Materials Engineering, Nanjing 211100, People's Republic of China; **Wen-Jiao Pei**, Institute of Advanced Materials and Forming Technology, NUAA, Nanjing 211100, People's Republic of China; **Xiao-Bin Tang**, Jiangsu Key Laboratory of Nuclear Energy Equipment Materials Engineering, Nanjing 211100, People's Republic of China; and College of Material Science and Technology, Nanjing University of Aeronautics and Astronautics, Nanjing 211100, People's Republic of China. Contact email: guoxunzhong@nuaa.edu.cn.

Table 1 The chemical compositions of P11 alloy steel (mass fraction, %)

Element	C	Mn	Si	Cr	Mo	P	S
Wt.%	0.05-0.15	0.30-0.60	0. 5-1.0	1.00-1.50	0.44-0.65	≤ 0.025	≤ 0.025

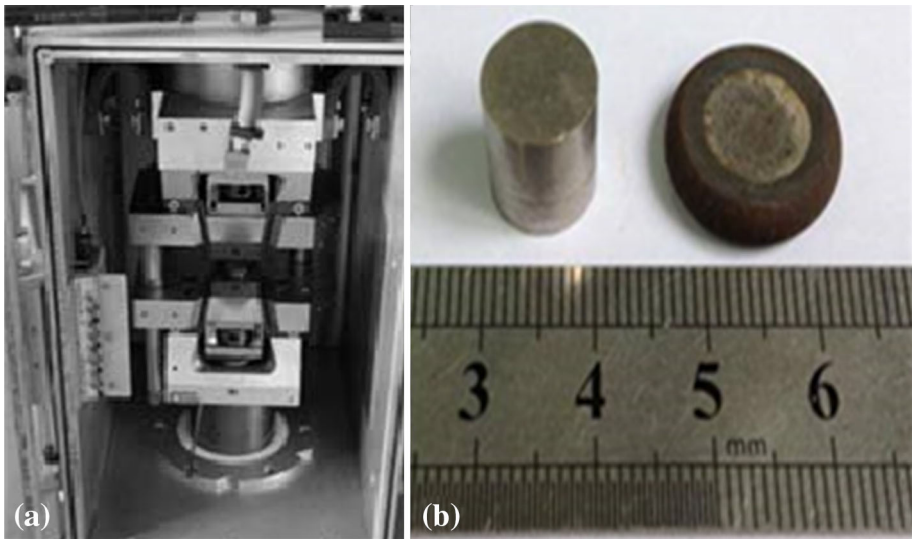

Fig. 1 Hot compression tests: (a) Gleeble-3500 system; (b) hot compression tests specimen

Table 2 Properties of P11 alloy steel

Yield strength, MPa	Compressive strength, MPa	Compression ratio, %	Modulus of elasticity, GPa	Poisson's ratio	Density, g/cm^3
250 ± 3.02	510 ± 4.84	32 ± 0.71	206 ± 3.51	0.3	7.85

of hot compression, the nonuniform deformation usually occurs due to the large friction between the specimens and the die. Therefore, a tantalum foil, with thickness of 0.1 mm, and high-temperature lubricant were placed between the specimen and the die to reduce the friction. The properties of P11 alloy steel measured by hot compression testing are presented in Table 2.

After the completion of hot compression experiments, the various specimens were sectioned perpendicular to the longitudinal axis. The specimens were polished and etched to observe the microstructure. Thin foils of 0.5 mm thickness were ground, thinned, and examined through transmission electron microscopy (TEM, Tecnai F 30).

2.1 Effects of Strain Rate on Flow Stress

The hot compression testing true stress-strain curves of P11 alloy steel, under different deformation conditions, are presented in Fig. 2. It is clear that, first, the flow stress increases rapidly, and then reaches a steady state with the further increase of the strain. Moreover, a typical flow stress peak in the true stress-strain curve of P11 alloy steel was not observed. During the initial stage of the hot compression experiment, the dislocation density increases significantly with the increase of deformation. At this stage, the work hardening of P11 alloy steel is the predominant strengthening mechanism, as the dislocations motions is restricted due to the interaction effects of the dislocations. Therefore, the rapid increment of stress occurs during this stage. However, with the increase in the dislocation density as deformation progresses, the storage energy becomes the driving force for the recovery and recrystallization of the materials. Thus, the above-mentioned phenomenon caused the overall flow softening of P11 alloy steel. When the flow softening effect gradually counteracted the work hardening effect, the flow stress reaches the steady state (Ref 10, 11).

Figure 2 also reveals the significant influence of strain rate on flow stress. Under the same conditions of temperature and strain, the flow stress level increases with the increasing strain rate, indicating that the P11 steel alloy is a positive strain rate-sensitive material. The effect of strain rate on the true stress-strain curve can be examined by investigating the relationship between dislocation motion and shearing stress during the deformation process. The relationship between the dislocation velocity and shearing stress is expressed using Eq 1 as follows:

$$V = V_0 \exp\left(-\frac{A}{\tau T}\right), \quad \text{(Eq 1)}$$

where V_0 is the dislocation velocity in the standard state; V is the dislocation velocity; A is the activation energy; τ is shearing stress; and T is the temperature.

The dislocation velocity increases with the increase of the strain rate. Eq 1 indicates that the shearing stress is positively affected by strain rate. Also, the shearing stress directly affects the flow stress. Therefore, the flow stress increases by increasing the strain rate. Furthermore, the inadequacy of the plastic deformation by the large strain rate also leads to the

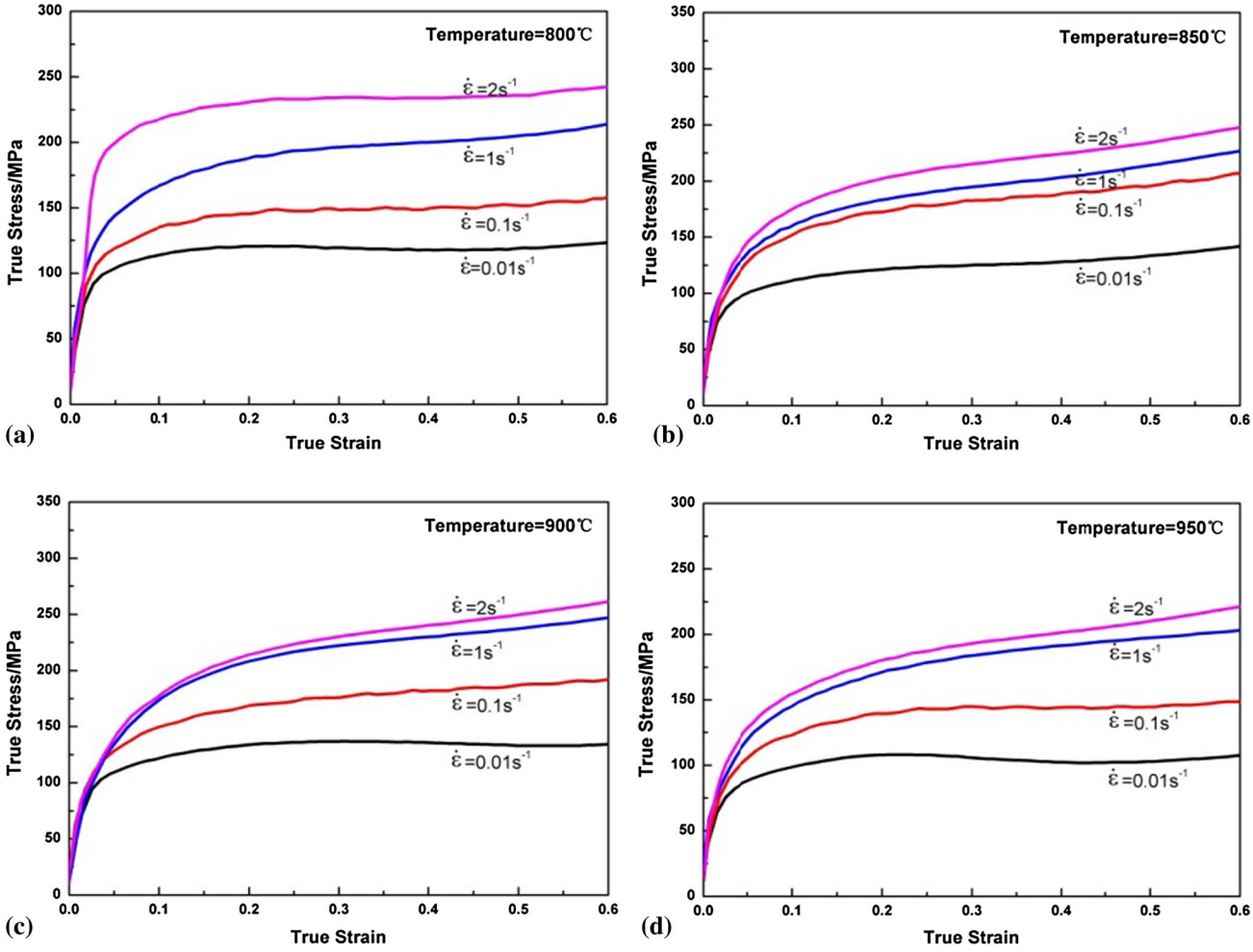

Fig. 2 The True stress-strain curves for P11 alloy steel under the different deformation conditions: (a) 800 °C; (b) 850 °C; (c) 900 °C; (d) 950 °C

increase of the flow stress. When the strain rate is relatively high, the elastic deformation plays an important role in the total deformation. The following obvious work hardening behavior results in the increment of flow stress. Moreover, there is no sufficient time for DRX, under the higher strain rates, which diminishes the softening effect and increases the flow stress.

2.2 Critical Strain of DRX

In the hot compression tests of constant strain rate, the DRX is traditionally identified by the presence of the stress peaks in the flow curves. The curves without the presence of clear characteristic peaks are, in general, considered related to the dynamic recovery effect. However, Poliak and Jonas reported that, not all the stress-strain curves of the materials display the peaks obtained by compression testing (Ref 12, 13). Therefore, the stress peak is not an essential condition for the determination of DRX in the hot compression testing (Ref 14).

The critical value of DRX obtained from the stress-strain curve is an important indicator to investigate the characteristics of DRX. The characteristics of DRX of the materials could be analyzed through the relationship between work hardening rate and flow stress. According to previous studies (Ref 15, 16), the critical conditions for DRX are calculated using Eq 2:

$$\frac{\partial}{\partial\sigma}\left(-\frac{\partial\theta}{\partial\sigma}\right)=0,\ \theta=\left(\frac{d\sigma}{d\varepsilon}\right)_{\varepsilon,T}, \quad \text{(Eq 2)}$$

where work hardening rate is the rate of change of stress against strain, when the strain rate and deformation temperature are kept constant, that is $\theta=\frac{\partial\sigma}{\partial\varepsilon}$. To explicitly describe the critical strain of the DRX, the minimum value of $\frac{\partial\sigma}{\partial\varepsilon}$ should be defined. The strain hardening rate should be determined from the true stress-strain curve to define the critical stress and critical strain of the DRX.

Figure 3(b)-(d) present the work hardening curves of the P11 alloy steel under the deformation temperature of 900 °C and strain rates of 0.01, 0.1, 1, and 2/s, respectively (Ref 17). Figure 3(b) and (c) clearly shows that the strain hardening rate sharply decreases from the maximum value and gradually reaches the minimum value, as the stress is increased. The value of the lowest point of the curve is the critical stress σ_c of DRX, and the corresponding critical strain of σ_c is ε_c. Further, the critical strain ε_c of DRX is determined by the inflection point of the curve, as shown in Fig. 3(d).

In order to successfully perform the hot push bending process, the process parameters must be adjusted carefully multiple times. The traditional method of the experiments by

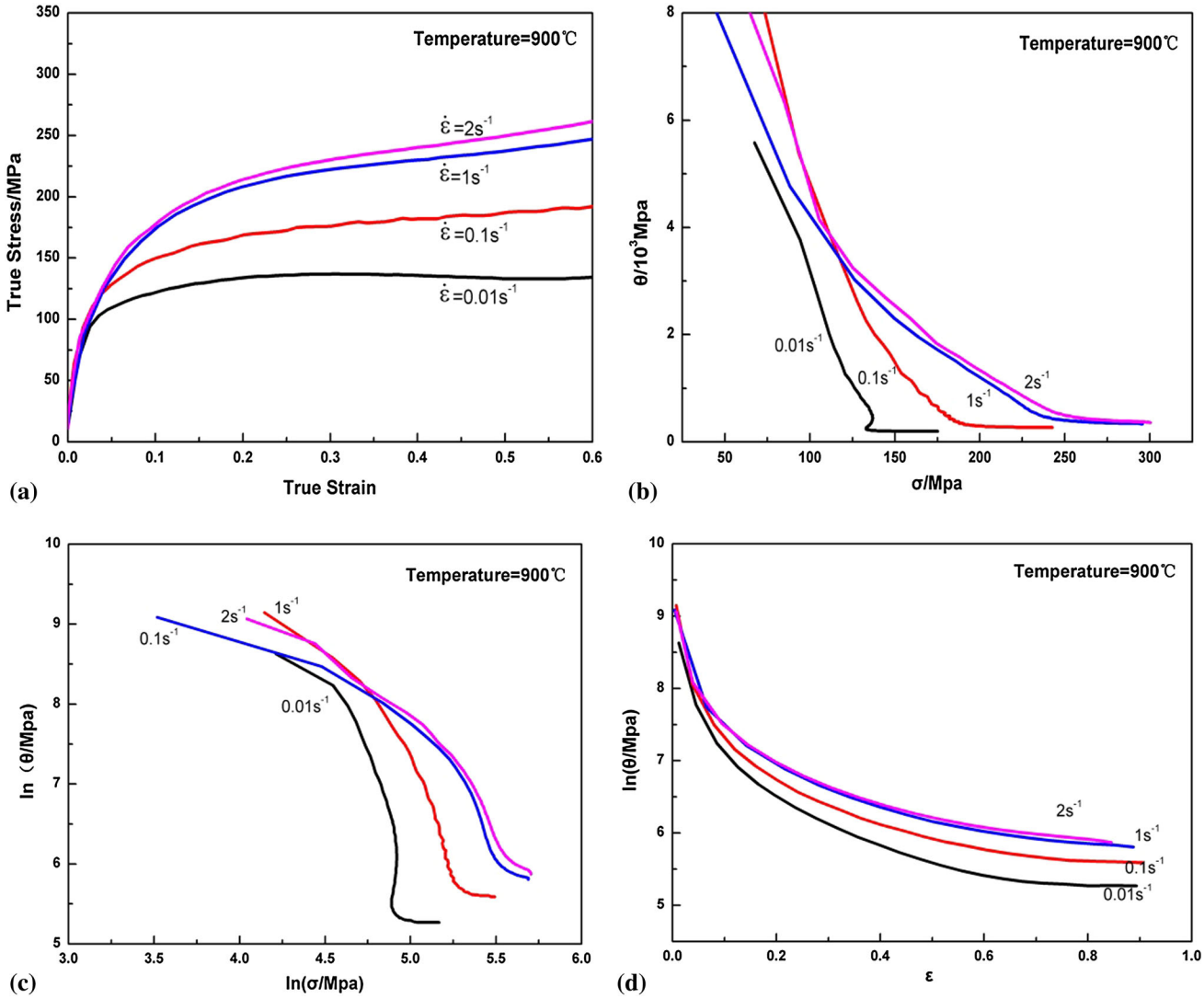

Fig. 3 Different of P11 alloy steel compressed at 900 K: (a) σ-ε curve; (b) θ-σ curve; (c) lnθ-lnσ curve; (d) lnθ-ε curve

Table 3 Tensile performance parameters of the bending tube

Sample	Elongation, %	Yield strength, MPa	Tensile strength, MPa
Outer arc	31.76 ± 0.66	330.62 ± 3.12	503.04 ± 4.92
Neutral layer	28.62 ± 0.59	359.44 ± 3.77	489.41 ± 4.01

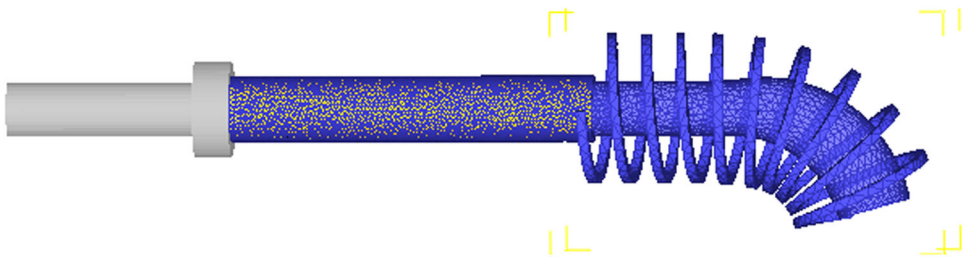

Fig. 4 FE model of hot push bending process

trial and error will be costly. Numerical simulation can narrow down to the optimum parameters which reduce the experimental time. It is first important to import the material model into the Computer-Aided Engineering software and then to obtain accurate simulation results. The high-temperature constitutive equation of the material model was built as described in Eq 3:

$$\dot{\varepsilon} = 5.091 \times 10^5 \times [\sinh(0.0063\sigma)]^{6.1372} \exp(-153812.7/RT). \quad \text{(Eq 3)}$$

3. Results and Discussions

3.1 FE Simulation Model

Parameters such as feed speed, heating frequency, and electric current density were optimized by finite element (FE) simulation. The FE model of hot push bending process is presented in Fig. 4. In general, the billet temperature distribution is not uniform in the axial direction (Fig. 5). The temperature of part squeezed into the induction coiler is higher than that of the other parts. In addition, the temperature distribution is different across the hoop direction, which is caused by the different heat density in the inner and the outer arc of the pipe blank. It is clear that, the temperature distribution is a complicated phenomenon for both the axial and hoop direction. Therefore, it is necessary to build the local dynamic induction heating model of the hot push bending process. The model includes the punch, pipe blank, induction coiler, and the mandrel. To obtain accurate simulation results, the tube, the induction coiler, and the mandrel were meshed using the tetrahedron element. In this model, tube temperature occurs dynamically (heated across the bending section) and cooling begins when it leaves the induction coiler.

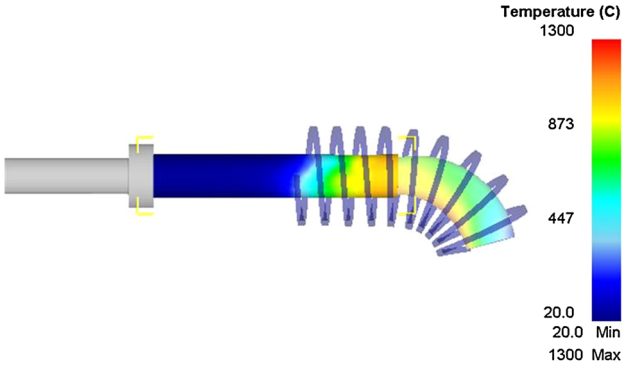

Fig. 5 Temperature field distribution during simulation process

3.2 Effects of Feed Speed on the Quality of Bend Tube

To investigate the effects of feed speed on the quality of the hot push bending tube, four different feeding speeds were selected, i.e., 0.5, 5, 10, and 20 mm/s. Applying the lower feeding speed, the tube requires higher time to be heated, which will increase the friction force between the softening material and the mandrel. The sections that were compressed were subjected to axial thrust and friction force. Later stacking and folding of material will generate in those sections as demonstrated in Fig. 6(a). However, larger strain rate is always generated at the higher feeding speed (20 mm/s). As presented in Fig. 2, the larger strain rate will lead to the increase of material deformation resistance and stress concentration in the inner arc of the bend tube. Figure 6(b), (c) shows that the quality of bend tube is quite good with appropriate feeding speed (5, 10 mm/s). By taking the high cost of the fast feeding

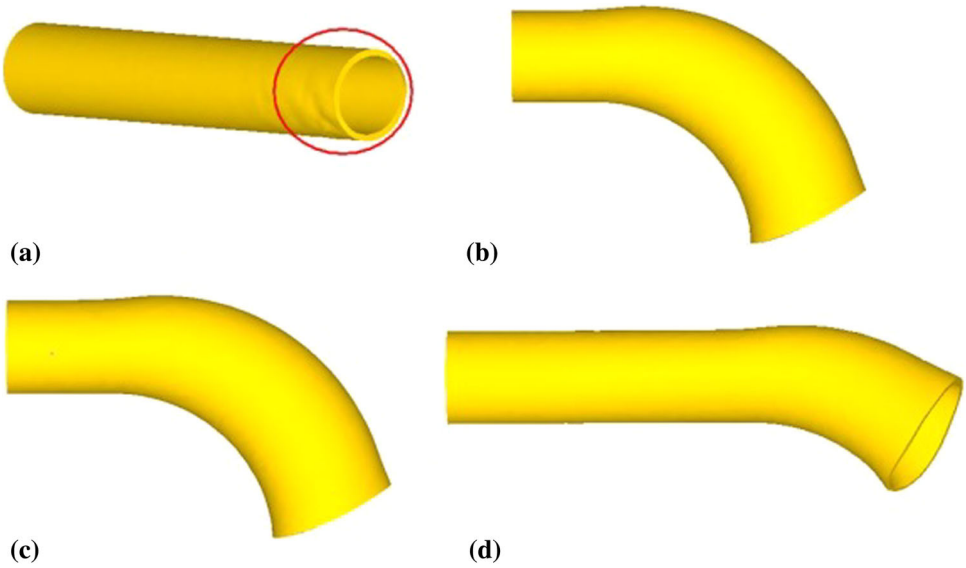

Fig. 6 Simulation results of different feed speeds: (a) 0.5 mm/s; (b) 5 mm/s; (c) 10 mm/s; (d) 20 mm/s

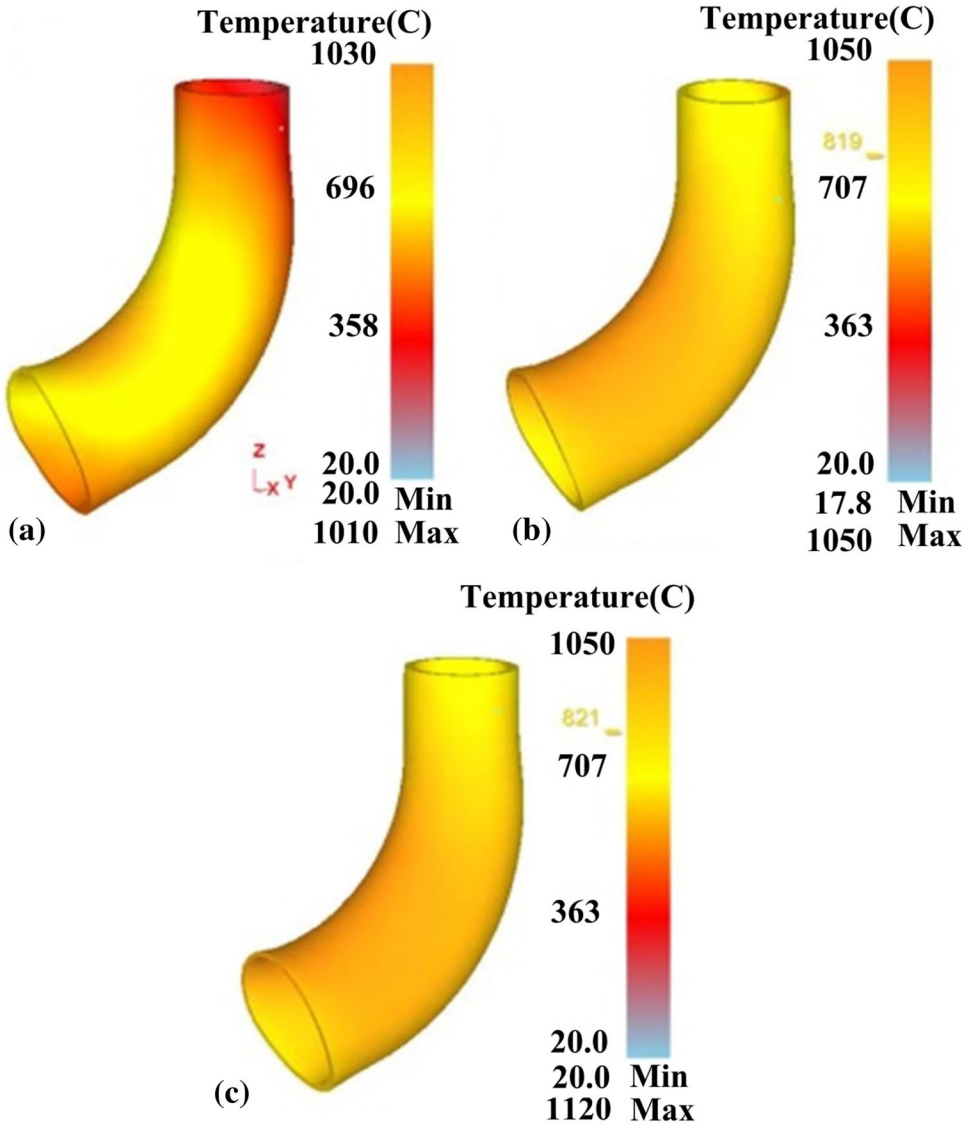

Fig. 7 Distribution of temperature field with the current density 10 A/mm^2: (a) 1000 HZ; (b) 1500 HZ; (c) 2000 HZ

speed into account, the lower feeding speed is more suitable for this process.

3.3 Effects of Heating Temperature on the Quality of Bend Tube

Heating temperature influences the hot push bending process profoundly, which includes heating frequency and current density. In order to study the effects of heating frequency on the quality of bending tube, heating frequency values of 1000, 1500, or 2000 Hz were utilized. Figure 7 shows the temperature field distribution of the different heating frequencies. It can be concluded that temperature of the tube billet was increased with the increase of heating frequency, and the maximum temperature was increased from 1010 to 1120 °C. In Fig. 7(a), the tube billet had been completely heated when the heating frequency was set at 1000 Hz, which satisfied the actual forming temperature (900 °C).

Four different current density values were selected to perform diverse heating efficiency, namely, 5, 10, 15, and 20 A/mm^2. Figure 8 shows the temperature field distribution of the different current densities. As presented in Fig. 8(a), lower current density led to uneven temperature field distribution where severe defects generated. The tube billet was thoroughly heated under a higher current density (10 A/mm^2), and the maximum temperature reached 1030 °C, which satisfied the actual forming temperature (900 °C). It can be also observed from Fig. 8(c), (d) that excessive current density will overheat the tube.

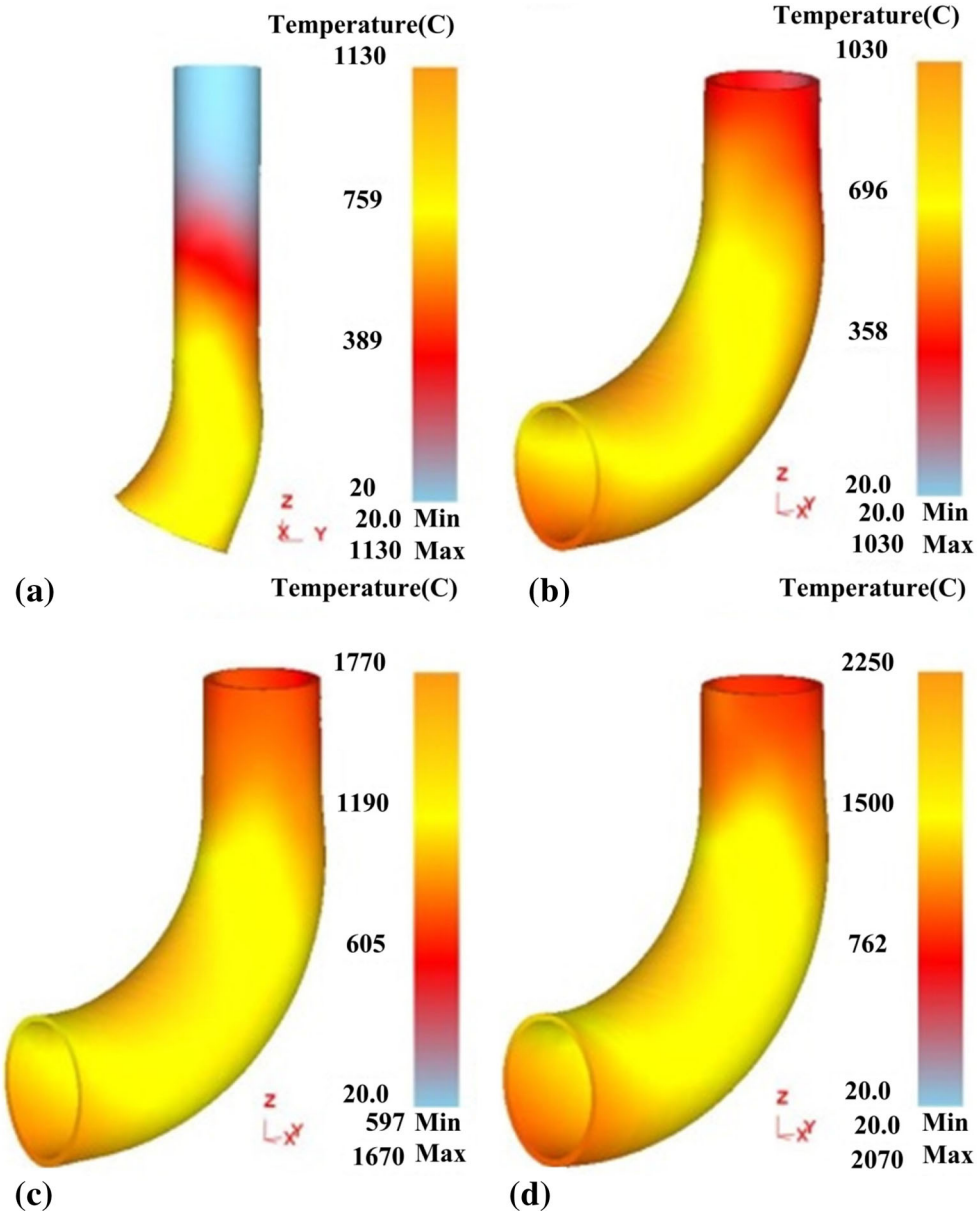

Fig. 8 Distribution of temperature field with the heating frequency 1000 Hz: (a) 5 A/mm^2; (b) 10 A/mm^2; (c) 15 A/mm^2; (d) 20 A/mm^2

3.4 Hot Push Bending Process of P11 Alloy Tube

Based on the simulation results, hot push bending experiments were carried out, as shown in Fig. 9, with a feeding speed of 5 mm/s, heating frequency of 1000 Hz, and current density of 10 A/mm^2. Figure 10 shows that the experimental results are in good agreement with the simulation results. Through observation and measurements, the surface quality of the bend tube is high, and the actual size was Φ 112 mm × 6.04 mm which meets the size requirements of Φ 114 mm × 6 mm.

Figure 11 shows a comparison of the thickness of the inner arc and outer arc between the simulation and experimental results. The simulation and experimental curves have similar trends. Figure 12 shows that the maximum cross-section

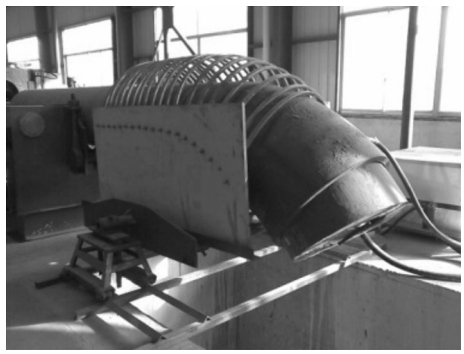

Fig. 9 Equipment of hot push bending process

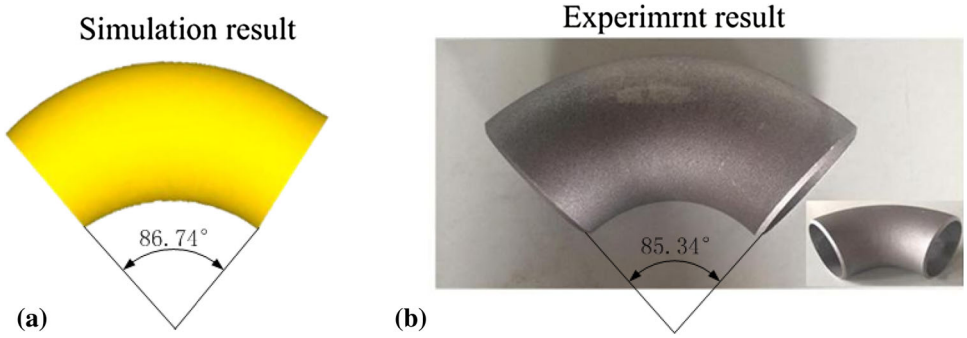

Fig. 10 Comparison between final experiment result with the simulation result

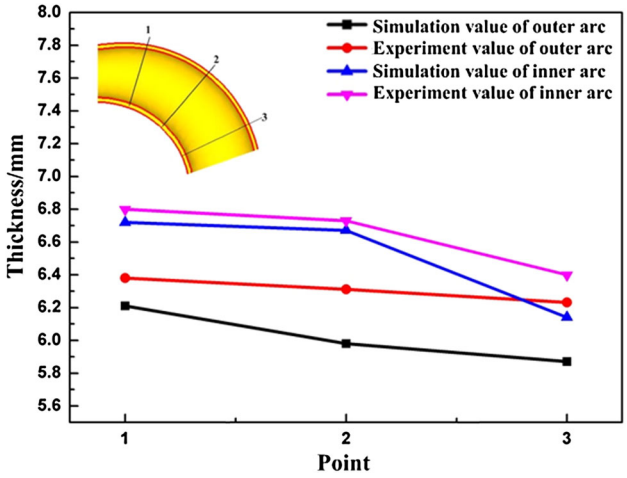

Fig. 11 Comparison of thickness between simulation and experiment results

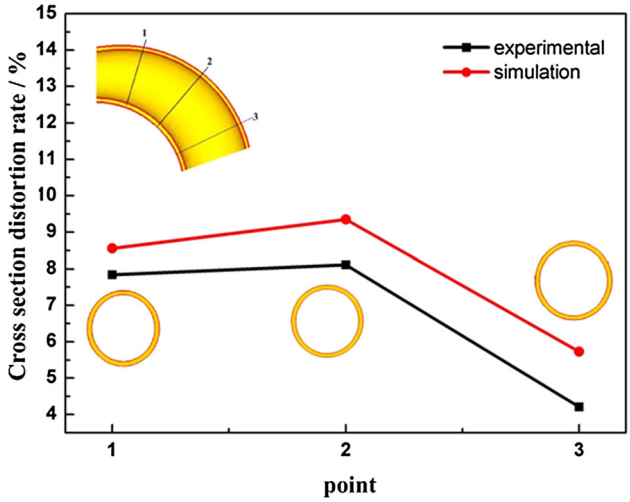

Fig. 12 Comparison of cross-section distortion rate between simulation and experiment results

distortion rates exist in enlargement section both of the simulation and experiment processes. The cross-section distortion rate was decreased with the tube billet entering into the fixed diameter section. There is the same regulation between the actual cross-section distortion rate distribution curve and the simulation curve.

3.5 Microstructure and Mechanical Properties

TEM images in Fig. 13 show the microstructure of the bend tube under different strain rates, which reveals that the microstructure of the alloy steel that was observed following hot deformation, changes with the decreasing strain rate. Most specifically, the number of dislocations was decreased and a recrystallized microstructure was formed. The low dislocation density of Fig. 13(a) should be attributed to the relatively low strain rate, which provides sufficient time for dislocations to climb and bypass any microstructural obstacles and rearrange. Correspondingly, fewer dislocations adjacent the grain boundaries resulted in the advantages related to the nucleation and grain growth during the recrystallization. Furthermore, fine recrystallization grains were gradually formed by the merging of the poorly orientated grains and by the growth of the subgrains (Ref 18, 19). The lower deformation time limited the climbing and bypassing of dislocations and hindered the release of the stored energy, resulting to the generation of dislocation walls. Therefore, there was a relatively large dislocation density in the grains, as shown in Fig. 13(c), (d).

Figure 14 shows the microstructure of the neutral layer, the outer arc, and the inner arc. It can be deduced from the change of grains size that DRX was activated during the hot push bending process. The crystalline grains were relatively evenly distributed in Fig. 14(a). The crystalline grains of Fig. 14(b) were elongated in a certain direction and the average size of those grains was higher than that of the grains of Fig. 14(a), (c). The tensile stress inflicted on the outer arc was considered to be the reason for this phenomenon. For the same reason, the compressive stress exerted on the inner arc resulted in the prodigious refinement of crystalline grains. Table 3 shows the mechanical properties of the outer arc and the neutral layer. It is clear that the elongation and the tensile strength were decreased with grain refinement. The reason is the increase of yield ratio that reduced the ductility of the material.

In order to analyze the grain orientation and texture of the deformed alloys after hot push bending process, EBSD analysis was performed on the deformed alloys, which were located in the inner and outer arc of the bending tube. As presented in Fig. 15, the low-angle misorientation was increased compared

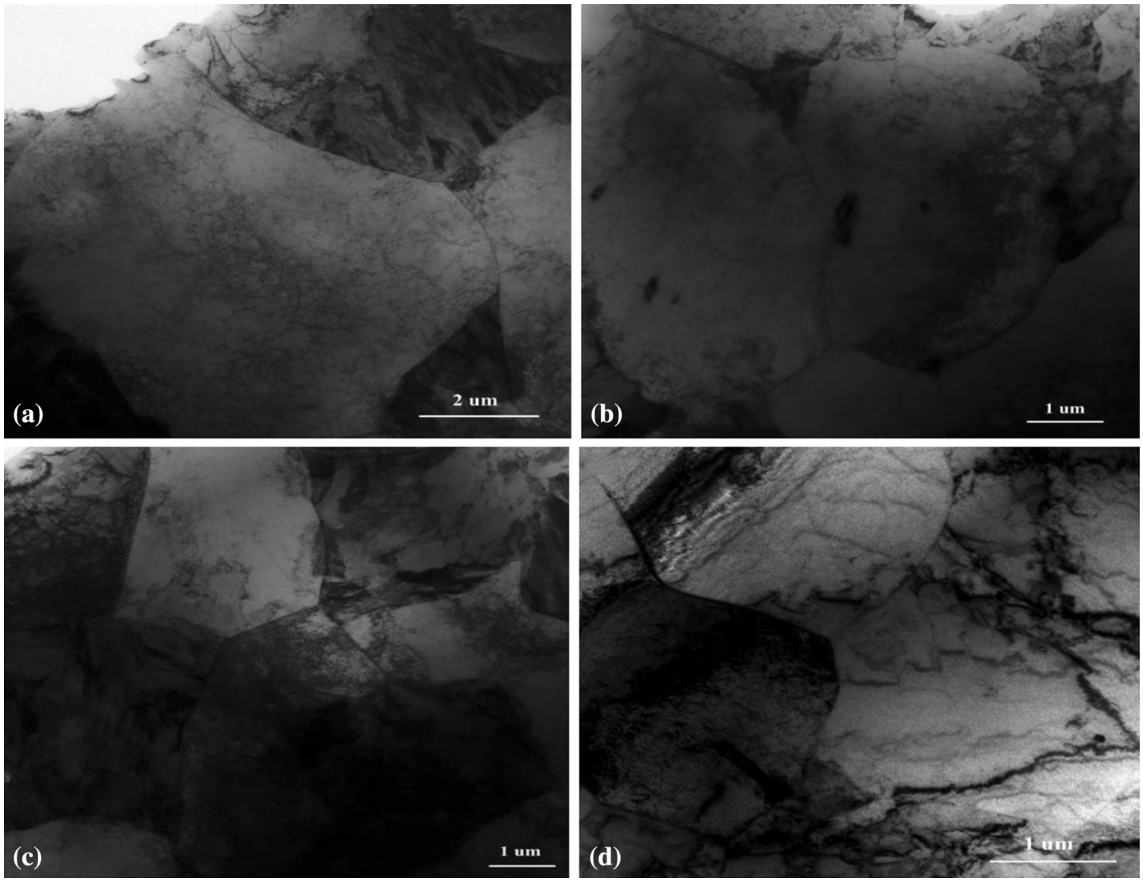

Fig. 13 TEM images under different feed speed at 1000 °C: (a) strain rate 0.01/s; (b) strain rate 0.1/s; (c) strain rate 1/s; (d) strain rate 2/s

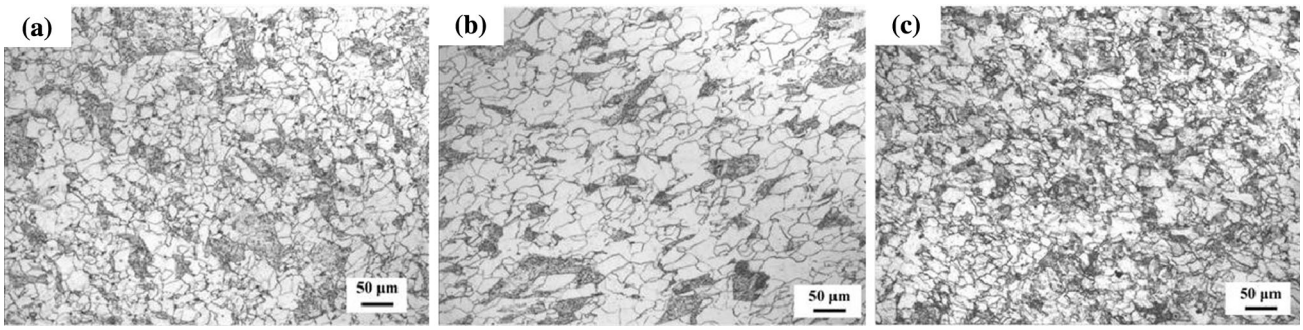

Fig. 14 Microstructure of typical positions (200×): (a) Neutral layer; (b) outer arc; (c) inner arc

to the random distribution of grain orientation (the black lines). This illustrates that the grain deformation occurred during the bending process. Figure 16 shows the grain diameter and IPF *X* coloring of both the inner and outer arcs. The grains below 5 μm account for the vast majority as presented in Fig. 16(a), (b). In addition, it can be calculated by EDAX-TSL that the green part is the main color in Fig. 16(c), (d), which means most of the grains in direction of $\{101\}//X$ are equiaxed grains, where *X* is the pushing direction. The cause of this phenomenon is considered to be DRX. As shown in Fig. 17, the outer arc was textured in the $\langle 111\rangle//ND$ direction, which is more concentrated than inner arc, where ND is the radial direction.

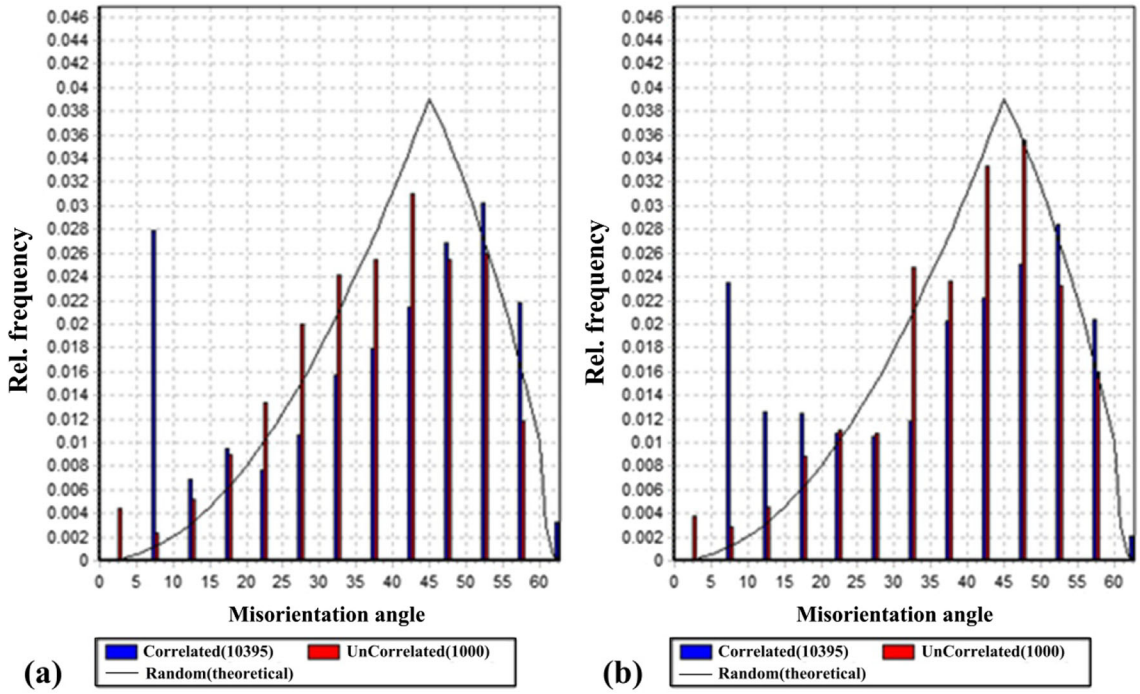

Fig. 15 Misorientation angle distribution: (a) inner arc; (b) outer arc

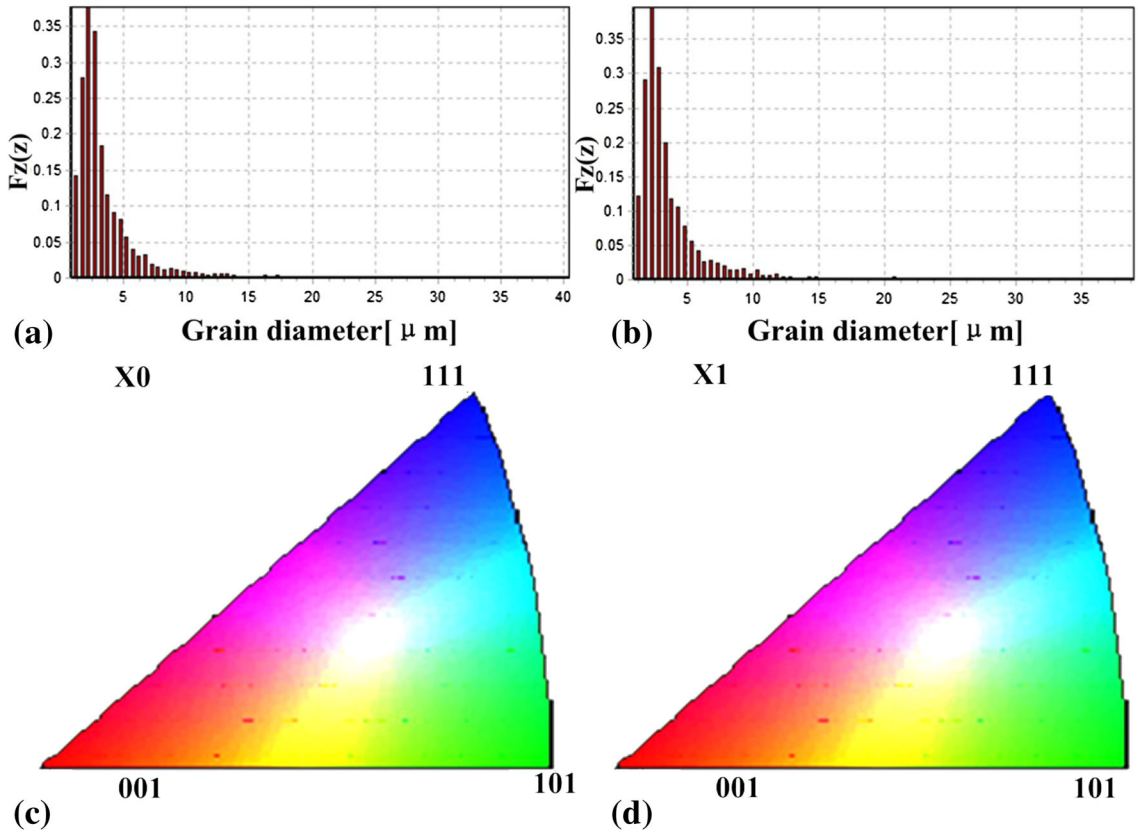

Fig. 16 Grain diameter and IPF X coloring: (a) grain diameter of inner arc; (b) grain diameter of outer arc; (c) IPF *X* coloring of inner arc; (d) IPF *X* coloring of outer arc

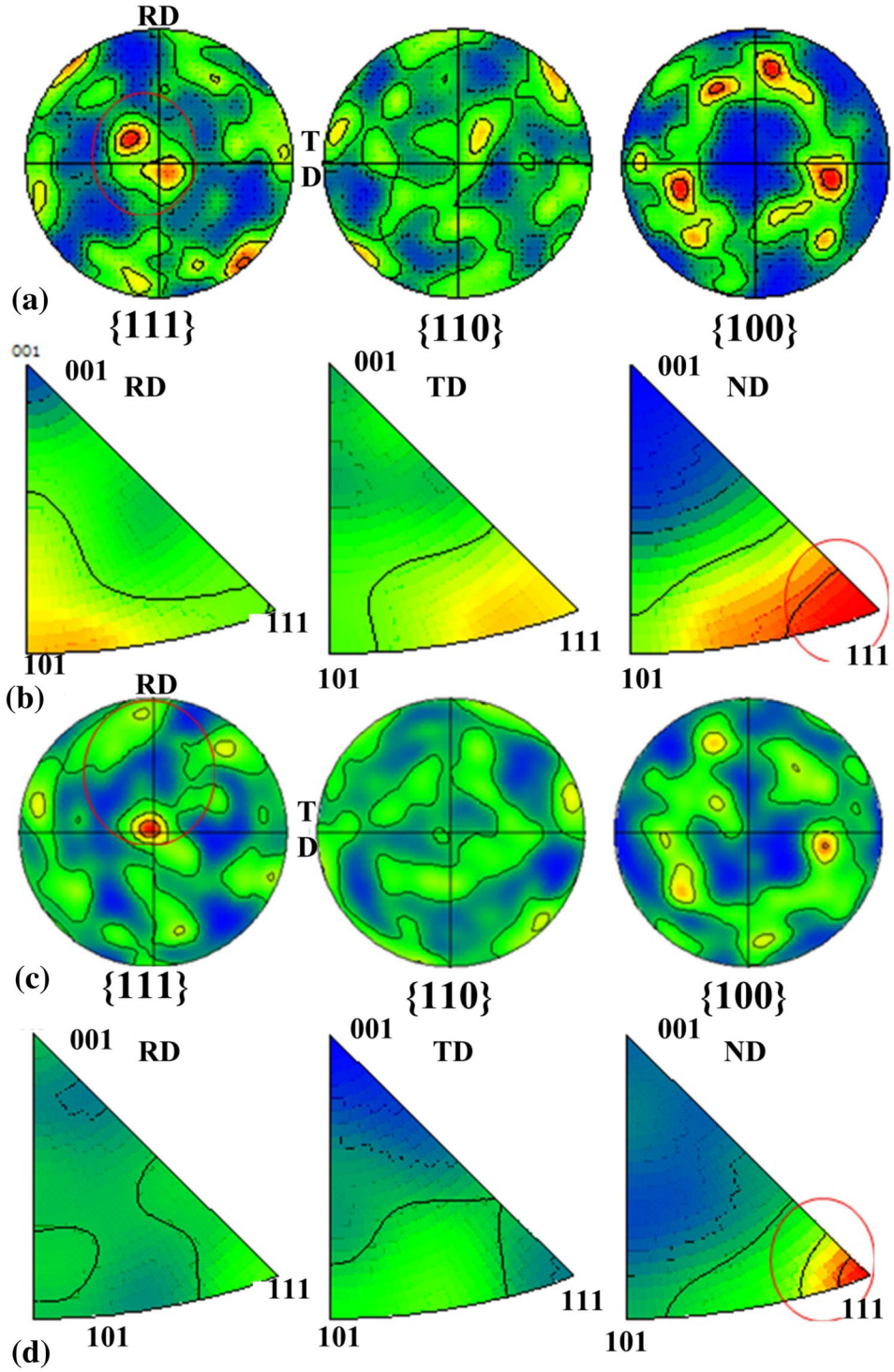

Fig. 17 Pole figure and inverse pole figure: (a) pole figure of inner arc; (b) inverse pole figure of inner arc; (c) pole figure of outer arc; (d) inverse pole figure of outer arc

4. Conclusions

(1) The flow stress of P11 alloy steel was increased with the augment in the strain rate; thus, the P11 alloy steel was a positive strain rate-sensitive material. P11 alloy steel did not display the typical peaks on the true stress-strain flow curves. However, the occurrence of DRX was observed in the plots of the strain hardening rate θ as a function of stress σ and $\ln\theta$-$\ln\sigma$ as a function of $\ln\theta$-ε. The results were confirmed by the observations of the microstructure of P11 alloy steel.

(2) The results of microstructure analysis indicated that the

strain rates were significantly affected by DRX in the hot deformation process. The size and volume fraction of DRX was increased and the dislocation density decreased with the decrease of strain rate.

(3) Due to recrystallization and difference in stress state, the crystalline grains of inner arc are superior to grains of outer arc and the neutral layer. However, outer arc performs better than the neutral layer in elongation and tensile strength, which is considered to be attributed to the increase of yield ratio.

Acknowledgments

The present study has been supported by the Natural Science Foundation of Jiangsu Province (Grant No. SBK2015022427), the Fundamental Research Funds for the Central Universities. (No. NJ20150023, No. NJ20160035, and No. NJ20160036).

References

1. G. Harrop and B.P. Poirier, Construction of Westinghouse AP1000 Nuclear Power Plants in China[J], *Int. Conf. Nucl. Eng.*, 2010, **6**, p 303–309
2. H. Mirzadeh and A. Najafizadeh, Prediction of the Critical Conditions for Initiation of Dynamic Recrystallization [J], *Mater. Des.*, 2010, **31**, p 1174–1179
3. M.A. Mostafaei and M. Kazeminezhad, Analyses on the Flow Stress of an Al-Mg Alloy During Dynamic Recovery [J], *J. Mater. Eng. Perform.*, 2013, **22**, p 700–705
4. Takanori Matsui, High Temperature Deformation and Dynamic Recrystallization Behavior of Alloy 718 [J], *Mater. Trans.*, 2013, **54**, p 512–519
5. G.Z. Quan, A. Mao, G.C. Luo et al., Constitutive Modeling for the Dynamic Recrystallization Kinetics of As-Extruded 3Cr20Ni10W2 Heat-Resistant Alloy Based on Stress-Strain Data [J], *Mater. Des.*, 2013, **52**, p 98–107
6. E.I. Poliak and J.J. Jonas, A One-Parameter Approach to Determining the Critical Conditions for the Initiation of Dynamic Recrystallization [J], *Acta Mater.*, 1996, **44**, p 127–136
7. J. Luo, M.Q. Li, W.X. Yu et al., Effect of the Strain on Processing Maps of Titanium Alloys in Isothermal Compression [J], *Mater. Sci. Eng. A*, 2009, **504**, p 90–98
8. S. Mandal, V. Rakesh, P.V. Sivaprasad et al., Constitutive Equations to Predict High Temperature Flow Stress in a Ti-Modified Austenitic Stainless Steel [J], *Mater. Sci. Eng. A*, 2009, **500**, p 114–121
9. J.J. Jonas, X. Quelennec, L. Jiang et al., The Avrami Kinetics of Dynamic Recrystallization [J], *Acta Mater.*, 2009, **57**, p 2748–2756
10. Y.C. Lin, M.S. Chen, J. Zhong et al., Effect of Temperature and Strain Rate on the Compressive Deformation Behavior of 42CrMo Steel [J], *J. Mater. Process. Technol.*, 2008, **205**, p 308–315
11. Y.H. Xiao and C. Guo, Constitutive Modelling for High Temperature Behavior of 1Cr12Ni3Mo2VNbN Martensitic Steel [J], *Mater. Sci. Eng. A*, 2011, **528**, p 5081–5087
12. E.I. Poliak and J.J. Jonas, Initiation of Dynamic Recrystallization in Constant Strain Rate Hot Deformation [J], *ISIJ Int.*, 2003, **43**, p 684–691
13. A. Najafizadeh and J.J. Jonas, Predicting the Critical Stress for Initiation of Dynamic Recrystallization [J], *ISIJ Int.*, 2006, **46**, p 1679–1684
14. A. Galiyev, R. Kaibyshev, and G. Gottstein, Correlation of Plastic Deformation and Dynamic Recrystallization in Magnesium Alloy ZK60 [J], *Acta Mater.*, 2001, **49**, p 1199
15. H.J. McQueen, S. Yue, N.D. Ryan et al., Hot Working Characteristics of Steels in Austenitic State [J], *J. Mater. Process. Technol.*, 1995, **53**, p 293–310
16. S.F. Medina and C.A. Hernandez, Modelling of the Dynamic Recrystallization of Austenite in Low Alloy and Microalloyed Steels [J], *Acta Mater.*, 1996, **44**, p 165–171
17. G.Z. Quan, G.S. Li, T. Chen et al., Dynamic Recrystallization Kinetics of 42CrMo Steel During Compression at Different Temperatures and Strain Rates [J], *Mater. Sci. Eng. A*, 2011, **528**, p 4643–4651
18. Y. Zhang, X.Q. Zeng, C. Lu et al., Deformation Behavior and Dynamic Recrystallization of a Mg-Zn-Y-Zr Alloy [J], *Mater. Sci. Eng. A*, 2006, **428**, p 91–97
19. J.D. Robson and P.B. Prangnell, Predicting the Recrystallized Volume Fraction in AA7050 Hot Rolling Plate [J], *Mater. Sci. Technol.*, 2002, **18**, p 607–614